

Cite this: *J. Mater. Chem. A*, 2018, 6, 8886Received 9th February 2018  
Accepted 24th April 2018

DOI: 10.1039/c8ta01408f

rsc.li/materials-a

# Black phosphorus quantum dots as dual-functional electron-selective materials for efficient plastic perovskite solar cells†

Nianqing Fu,<sup>a</sup> Chun Huang,<sup>b</sup> Peng Lin,<sup>b</sup> Mingshan Zhu,<sup>c</sup> Tao Li,<sup>d</sup> Mao Ye,<sup>b</sup> Shenghuang Lin,<sup>d</sup> Guoge Zhang,<sup>a</sup> Jun Du,<sup>a</sup> Chang Liu,<sup>e</sup> Baomin Xu,<sup>e</sup> Danyang Wang<sup>f</sup> and Shanming Ke<sup>\*b,g</sup>

Organic–inorganic hybrid metal halide perovskite solar cells (PSCs) have attracted tremendous research interest due to their high power conversion efficiency and simple fabrication. However, the exploitation of new electron-selective materials which can simultaneously tailor the quality of metal halide perovskite film for low-temperature-produced plastic organic–inorganic halide perovskite solar cells (PSCs) is of key importance but remains a great challenge. Herein, facile solution-processed black phosphorus quantum dots (BPQDs) with ambipolar conductivity are developed as dual-functional electron-selective layer (ESL) in plastic PSCs. The BPQD ESL plays crucial roles in both forming a cascade energy level for fast electron extraction and guiding the crystallization behavior of the perovskite to yield compact perovskite films with less traps, good crystallization and ordered orientation. The perovskite films deposited on the BPQD ESL exhibit excellent optoelectronic properties, and the resulting plastic planar perovskite solar cells possess a reasonably high efficiency of 11.26%. The 3.15-fold enhancement in efficiency arises from both the efficient electron extraction and suppressed radiative and trap-assisted non-radiative recombination compared with the devices built on the bare ITO surface without an ESL. This work paves a promising way for developing novel electron-selective non-oxide materials for highly efficient solar cells.

## 1. Introduction

Organic–inorganic halide perovskite solar cells (PSCs) have revolutionized photovoltaic technology as their power conversion efficiency has been raised dramatically, from 3.8% in 2009 to 22.1% in 2016.<sup>1,2</sup> Thus far, TiO<sub>2</sub> is deemed as the most successful ESL of delivering high efficiency for PSCs.<sup>2–4</sup> However, the mobility of TiO<sub>2</sub> is at least two orders of magnitude lower than that of other components, namely, perovskite and hole transport layer, of PSCs,<sup>3,4</sup> and is the primary limitation for further improvement in efficiency. More importantly, TiO<sub>2</sub> catalyzes the decomposition of organic–inorganic perovskite under ultraviolet irradiation and leads to serious instability of the devices.<sup>5,6</sup> A high-quality TiO<sub>2</sub> ESL often requires sophisticated high-temperature treatment above 450 °C or high-vacuum process (*e.g.* sputtering, pulsed laser deposition),<sup>7</sup> which act as barriers to the low-cost and fast mass production of PSCs for commercialization. Moreover, the high-temperature process is excluded when the devices are designed on plastic substrate for flexible solar cells, which have the merits of light weight, flexibility, suitability for roll-to-roll manufacturing, and convenience of integration.<sup>7–9</sup> Recently, many efforts have been devoted to developing some substitutes, including fullerene and its derivatives,<sup>10,11</sup> organic molecules,<sup>12</sup> solid-state ionic liquid and a series of metal oxides/sulfides (*e.g.* Al<sub>2</sub>O<sub>3</sub>, ZnO, SnO<sub>2</sub>, WO<sub>x</sub>, Nb<sub>2</sub>O<sub>5</sub>, In<sub>2</sub>O<sub>3</sub>, Zn<sub>2</sub>SnO<sub>4</sub>, In<sub>2</sub>S<sub>3</sub>, *etc.*)<sup>13–22</sup> to replace TiO<sub>2</sub> as ESL for low-temperature processed rigid or flexible PSCs (see more detailed information in Table S1 in ESI†). Among them, fullerene and its derivatives show excellent performance in PSCs. However, they are expensive, and the designed device configuration usually has to be restricted to an inverted structure mainly because of the wettability of those materials. ZnO and SnO<sub>2</sub>, which can be simply prepared by a cost-effective solution-processing technique, are the most common choices of metal oxides employed as ESL for low-temperature produced PSCs with promising performance. However, the thermal instability of ZnO is its biggest drawback affecting the stability of PSCs. In this regard, it is still crucial and urgent to develop

<sup>a</sup>School of Materials Science and Engineering, South China University of Technology, Guangzhou 510640, P. R. China. E-mail: msnqfu@scut.edu.cn

<sup>b</sup>Guangdong Research Center for Interfacial Engineering of Functional Materials, College of Materials Science and Engineering, Shenzhen University, Shenzhen 518060, P. R. China. E-mail: smke@szu.edu.cn

<sup>c</sup>School of Environment, Jinan University, Guangzhou 510632, P. R. China

<sup>d</sup>Department of Applied Physics, The Hong Kong Polytechnic University, Hong Kong, P. R. China. E-mail: shenghuanglinchina@gmail.com

<sup>e</sup>Department of Materials Science and Engineering, Southern University of Science and Technology, Shenzhen 518055, P. R. China

<sup>f</sup>School of Materials Science and Engineering, The University of New South Wales, Sydney, New South Wales 2052, Australia

<sup>g</sup>School of Materials Science and Engineering, Nanchang University, Nanchang 330031, Jiangxi, P. R. China

† Electronic supplementary information (ESI) available. See DOI: 10.1039/c8ta01408f

alternative ESL materials which can be obtained through a simple and low-temperature process, even though some impressive successes have already been achieved.

In the past few years, two-dimensional (2D) materials, such as graphene and transition-metal dichalcogenides (TMDs), have attracted tremendous interest as a class of promising materials for nanodevices, owing to their intriguing physical properties.<sup>22–25</sup> However, devices based on these materials suffer from some major drawbacks, such as the lack of a bandgap in graphene and the considerably low conductivity of TMDs.<sup>22,24,25</sup> As a new member of the 2D materials family, black phosphorus (BP), a rare allotrope of phosphorus, has recently attracted enormous attention due to its inherently fascinating features of high theoretical mobility, tunable direct bandgap, ambipolarity and simple fabrication.<sup>24,26–29</sup> The bandgap of BP can be tuned from 0.3 eV for bulk to nearly 2.0 eV for the monolayer form.<sup>24,28,29</sup> Moreover, when BP appears in the form of quantum dots, it exhibits more amazing and unique electronic and optical properties, owing to the quantum confinement and edge effects.<sup>25,29</sup> As an elemental semiconductor, BP shows ambipolar conductivity for both electron and hole.<sup>24,28,29</sup> The electron and hole mobility can be up to  $\sim 220$  and  $350 \text{ cm}^2 \text{ V}^{-1} \text{ s}^{-1}$  at room temperature, respectively, for its polycrystalline form.<sup>30</sup> The electron mobility of BP is roughly three orders of magnitude higher than that of  $\text{TiO}_2$  ( $0.1\text{--}4 \text{ cm}^2 \text{ V}^{-1} \text{ s}^{-1}$ ).<sup>31</sup> Very recently, both single- or few-layered phosphorene nanosheets and black phosphorus quantum dots (BPQDs) have been explored as promising materials for field-effect transistors,<sup>32</sup> photodetectors,<sup>33</sup> photocatalysis,<sup>34,35</sup> photoelectronics,<sup>36</sup> supercapacitors,<sup>37</sup> lithium/sodium ion batteries,<sup>38</sup> and solar cells.<sup>39–42</sup> Guo and Yan *et al.* exploited BPQDs as light-harvesting enhancer for dye-sensitized solar cells and organic photovoltaics (OPVs), respectively, to increase the light utilization.<sup>39,40</sup> Chen *et al.* demonstrated that the BPQD can be employed for interface modifications of the hole transport layer to enhance the charge extraction of solar cells.<sup>41</sup> Lau's work suggested that the modification of ZnO electron transport layer by BP flakes can promote electron extraction from the excited active film,<sup>42</sup> indicating the potential of BP as an electron-selective material. However, using BPQDs as ESL alone in solar cells, especially for the plastic ones, has never been reported.

In this work, we present that BPQDs, prepared by facile liquid exfoliation, show an ambipolar conductivity and were successfully exploited as dual-functional ESL for low-temperature-processed plastic PSCs. The crafted BPQDs can offer suitable energy bands to form a desired band alignment that facilitates electron extraction but rejects hole injection from the  $\text{FA}_{0.85}\text{MA}_{0.15}\text{PbI}_{2.5}\text{Br}_{0.5}$  perovskite to the ESL. Meanwhile, the BPQDs can facilitate the formation of dense perovskite film with good crystallization and ordered orientation, which reduces the trap state in the perovskite film and leads to suppressed recombination. The plastic PSCs based on our BPQD ESL achieved an efficient power conversion efficiency (PCE) of 11.26%, while the PCE is 14.6% for the FTO/glass-based rigid device. These results are promising when compared with the earlier attempts of using ESL materials for PSCs (Table S1†). This work demonstrates that the elemental material, BP, is a promising replacement for the existing ESL materials, such as metal oxides and organic molecules, for solar cells.

## 2. Experimental section

### 2.1. Materials

BP crystals were obtained from Smart Elements GmbH, Austria. Formamidinium iodide ( $\text{H}_2\text{N}=\text{CHNH}_2\text{I}$ ; FAI), methylammonium iodide ( $\text{CH}_3\text{NH}_3\text{I}$ ; MAI), methylammonium bromide ( $\text{CH}_3\text{NH}_3\text{Br}$ ; MABr),  $\text{PbI}_2$  and  $\text{PbBr}_2$  were purchased from Dyesol. *N,N*-Dimethylformamide (DMF, 99.9%), dimethyl sulfoxide (DMSO, 99.9%), 4-*tert*-butylpyridine (4-TBP, 96%), lithium bistrifluoromethane sulfonimide (LiTFSI, 99.9%), and chlorobenzene (99.5%) were obtained from Sigma-Aldrich. All chemicals were used as received without further purification.

### 2.2. Preparation of BPDQs

The BP crystals were ground into powder and added into NMP solution. Then, the mixtures were ultrasonicated using an ultrasonic bath (400 W) at  $20^\circ\text{C}$  for 8 h. The obtained BP mixture was purified by centrifugation, with a rate of 5000 rpm for 30 min, to remove larger particles. Then, the residual BP dispersion was further turned into BPQDs by probe sonication for 4 h.

### 2.3. Preparation of BPQD film and PSCs

Prior to film deposition, a designed pattern was etched onto the ITO/PEN substrate (Peccell) using Zn powder and 2 M HCl solution, then successively well cleaned with detergent, absolute ethanol and DI water. A subsequent 10 min  $\text{O}_2$  plasma treatment was conducted to increase wettability of the ITO surface. BPQD films were fabricated by spin-coating the freshly prepared BPQD IPA solution at 1500 rpm for 30 s in a  $\text{N}_2$ -filled glove box. The thickness of BPQD films was controlled by repeating the spin-coating process a certain number of times (*i.e.* 0, 1, 3, 5, and 7). Between each coating, the as-prepared film was dried at  $60^\circ\text{C}$  for 5 min. The  $\text{FA}_{0.85}\text{MA}_{0.15}\text{PbI}_{2.5}\text{Br}_{0.5}$  perovskite films were deposited on the newly coated BPQD film using a procedure according to the reported work.<sup>43</sup> The as-deposited films were heated at  $100^\circ\text{C}$  for 60 min for crystallization. For comparison, perovskite films were also deposited on the bare ITO/PEN or compact  $\text{TiO}_2$ -coated FTO/glass substrates under the same conditions. The high-temperature-sintered  $\text{TiO}_2$  compact layer was deposited according to our previous work.<sup>44</sup> A hole-transporting material (HTM) solution comprised by 61 mM spiro-OMeTAD, 55 mM *tert*-butylpyridine (TBP) and 26 mM Li-TFSI salt in chlorobenzene was spin-coated on the perovskite layer at 4000 rpm for 30 s. Au films with thickness of 80 nm were thermally evaporated on the electrodes, which were previously stored in a desiccator overnight, as the top electrode. The active area of each PSC is  $0.09 \text{ cm}^2$ .

### 2.4. Characterization

The morphology and structure of BPQDs were characterized by scanning transmission electron microscope (STEM, JEOL JEM-2100F) operated at 200 kV. The morphology of both the BPQDs on Si plate and BPQD films on ITO/PEN was imaged by AFM (Veeco Dimension-Icon system) with a scanning ratio of 0.977 Hz. The micrographs of the BPQD and perovskite films

were obtained using a field-emission scanning electron microscope (FESEM, ZEISS Merlin) operated at 5 kV. The optical absorption of BPQDs was studied by a UV-Vis spectrophotometer (Hitachi U-3010, Japan). Raman spectra were collected using a Horiba Jobin Yvon HR800 Raman microscopic system equipped with a 488 nm laser operating at 180 mW. The spot size of the excitation laser is  $\sim 1 \mu\text{m}$ . The PL measurements were conducted on a FLS920P Edinburgh Analytical Instrument apparatus with a 485 nm laser excitation source. Photocurrent density–voltage ( $J$ – $V$ ) curves were recorded using a Keithley 2400 source meter under one sun AM 1.5 G illumination ( $100 \text{ mW cm}^{-2}$ ) supplied by a solar simulator (Enlitech SS-F7-3A, 300 W). The light intensity was calibrated using a silicon reference cell (NREL) equipped with a power meter. The incident photon-to-electron conversion efficiency (IPCE) was tested using an IPCE system (Enlitech QE-R).

### 3. Results and discussion

#### 3.1. Morphological and optical properties of black phosphorus quantum dots

The crafted BPQDs were synthesized from the BP crystals by liquid-phase exfoliation, employing a combination of bath sonication and probe sonication in *N*-methyl-2-pyrrolidone (NMP). Fig. 1a shows the schematic crystal structure of BP, which is composed of layered orthorhombic structure with the space group of *Cmca* (no. 64). Each P atom bonds with three

others, and the thickness of each layer, along the  $y$  direction, is around  $5.3 \text{ \AA}$ .<sup>28,29</sup> Scanning transmission electron microscopy (STEM) and atomic force microscopy (AFM) were employed to explore the fine microstructural morphology of the as-prepared BPQDs. The STEM images shown in Fig. 1b and c depict the well-dispersed BPQDs with diameters ranging from 3 nm to 10 nm. The average crystallite size of BPQDs is found to be  $4.7 \pm 1.6 \text{ nm}$  (Fig. 1f). The atomic structure of individual BPQDs is further analyzed by high-resolution TEM (HRTEM). The interplanar spacing of the studied BPQDs is  $\approx 0.21 \text{ nm}$  (Fig. 1d and e), which can be assigned to the (002) crystal plane of orthorhombic phosphorus (ICDD-PDF: No. 76–1963). The AFM image showing the topographic morphology of BPQDs is displayed in Fig. 1g. The statistical average thickness of BPQDs is  $1.52 \pm 0.5 \text{ nm}$  (Fig. 1i), corresponding to a stack of  $3 \pm 1$  layers of BPs.

The optical properties of the obtained BPQDs were characterized by UV/Vis absorption spectroscopy, Raman spectroscopy and ultraviolet photoelectron spectrometry (UPS). The Raman spectra of as-prepared BPQDs and bulk BP are shown in Fig. 2a. Three feature peaks can be ascribed to one out-of-plane phonon mode of  $A_g^1$ , located at  $360.8 \text{ cm}^{-1}$ , and two in-plane modes of  $B_{2g}$  and  $A_g^2$ , located at  $438.6$  and  $466.1 \text{ cm}^{-1}$ , respectively.<sup>25,45</sup> Compared to the bulk BP, the  $A_g^1$ ,  $B_{2g}$  and  $A_g^2$  modes of BPQDs are red-shifted.<sup>25</sup> This red-shift phenomenon is similar to the model change of graphene quantum dots,<sup>46</sup> indicating the formation of thin BP fragments with small lateral dimensions.<sup>25</sup>

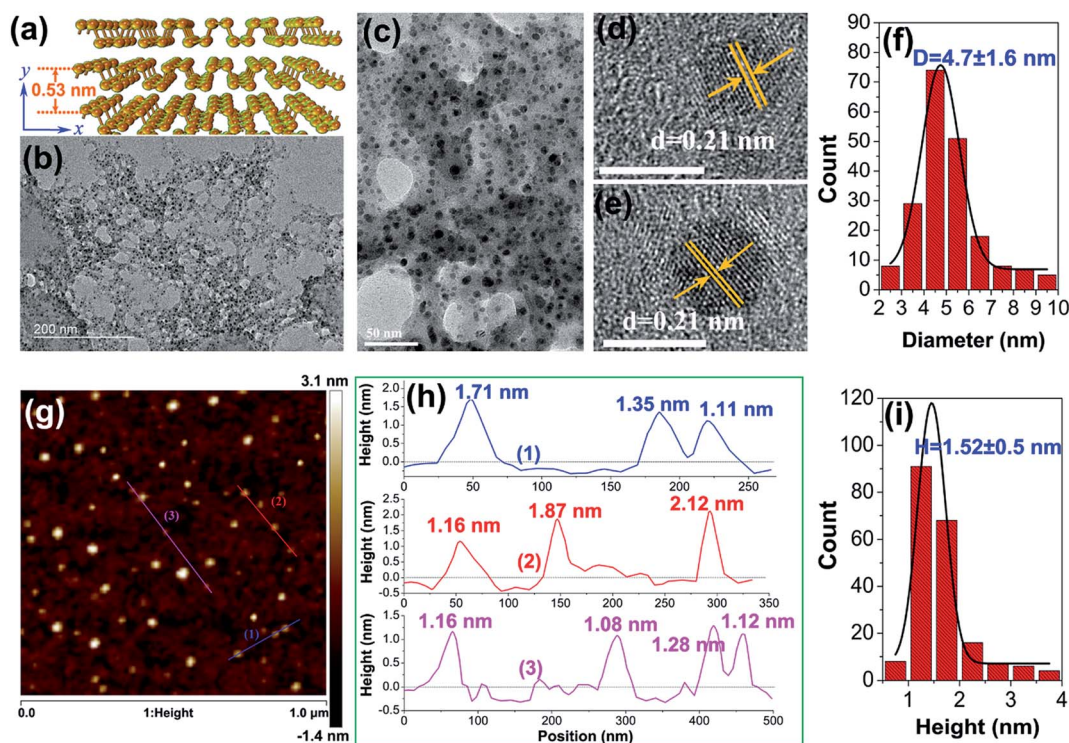


Fig. 1 Morphology and structure characterization of black phosphorus quantum dots (BPQDs). (a) Schematic diagram of layered crystal structure of bulk black phosphorus (BP); (b) TEM image of the BPQDs; (c) enlarged TEM image of BPQDs; (d and e) high-resolution TEM image showing the lattice fringe of BPQD, scale bar = 5 nm; (f) statistical distribution of the sizes of 200 BPQDs measured from TEM images; (g) AFM images of BPQDs on Si sheet; (h) height profiles along the lines marked in (g); (i) statistical distribution of the thickness of 200 BPQDs measured by AFM.

The prepared BPQDs can be easily dispersed in 2-propanol as a clear yellow liquid (inset of Fig. 2b). The absorption curve of the prepared solution is illustrated in Fig. 2b. To gain the exact bandgap energy ( $E_g$ ) value of the obtained BPQDs, a Tauc plot was evolved from the UV-Vis spectrum (see details in ESI†). According to the Tauc plot (Fig. 2c), the bandgap of BPQDs is deduced to be 1.9 eV, which is in line with the value determined from the photoluminescence (PL) spectrometry of BPQDs in isopropanol (Fig. S1†) and consistent with the reported values of BPQDs with similar size.<sup>40,41</sup> The valence band (VB) was evaluated by the VB spectrum from UPS measurements. For the UPS test, BPQDs were coated on the ITO/PEN substrate five times to form a dense film. As shown in Fig. 2d, the VB of BPQDs on ITO substrate is tested to be  $\sim 5.74$  eV. According to the above analysis, therefore, the conduction band (CB) and VB are 3.84 and 5.74 eV, respectively.

### 3.2. Photovoltaic performance of perovskite solar cells

The electron and hole transport behaviors of the obtained BPQDs were investigated by measuring the performance of the BPQD-based field effect transistor (FET). The transfer characteristics of the FET are measured at room temperature using the configuration presented as inset in Fig. S2a† (more experimental details for the FET test can be found in ESI†). Fig. S2† shows the transfer characteristics and  $I$ - $V$  curve of the BPQD FET. The source-drain  $V_{DS}$  was set at 0.1 V, while the backgate voltage  $V_G$  was varied from  $-20$  V to 50 V. The 'On/Off' ratio of  $\sim 1.38$  in drain current was observed. It can be found from the transfer characteristics that the BPQD FET also shows a clearly ambipolar conductivity, as indicated in BP flakes.<sup>47</sup> The hole

and electron mobility of BPQDs were estimated to be around  $1.48 \times 10^{-2}$  and  $7.8 \times 10^{-3} \text{ cm}^2 \text{ V}^{-1} \text{ s}^{-1}$ , respectively. Since the BPQDs demonstrate the fascinating advantages of ambipolar conductivity for both electron and hole as well as a sizable bandgap, we are motivated to exploit BPQDs as SEL for plastic PSCs, with the device architecture shown in Fig. 3a. Firstly, we assessed the possibility of BPQDs as ESL for PSCs from the energy level (*i.e.* conduction and valence band) point of view. The band alignment of the structured PSCs is sketched in Fig. 3b, which reveals that both CB and VB levels of the BPQDs films match well with those of  $\text{FA}_{0.85}\text{MA}_{0.15}\text{PbI}_{2.5}\text{Br}_{0.5}$  perovskite (3.8 and 5.4 eV for CB and VB, respectively) to form a cascade energy level, facilitating electron transfer but rejecting hole extraction from the absorber to the BPQD ESL.

The microstructure of the PSCs was imaged by scanning electron microscopy. The cross-sectional SEM image of the PSC device displayed in Fig. 3c showcases a well-defined layered structure with sharp interfaces. The thicknesses of BPQD ESL (5 layers), perovskite, Spiro-OMeTAD, and Au are around 30, 500, 160, and 80 nm, respectively. To uncover the effects of ESL thickness on the device performance, BPQD films with various thicknesses (*i.e.* 0, 1, 3, 5, 7 layers) were deposited by controlling the number of times spin-coating with BPQD solution was repeated. The current density-voltage ( $J$ - $V$ ) curves of the plastic PSCs with and without BPQD ESL are shown in Fig. 3d and S3.† The detailed photovoltaic parameters of devices with BPQD layers of different thicknesses are summarized in Table 1. For the PSCs without any ESL, *i.e.* the perovskite layer deposited directly on bare ITO, the device yields a low PCE of 3.58%. With the increase of BPQD thickness, all photovoltaic parameters gain a simultaneous improvement (Table 1). The PSCs built on

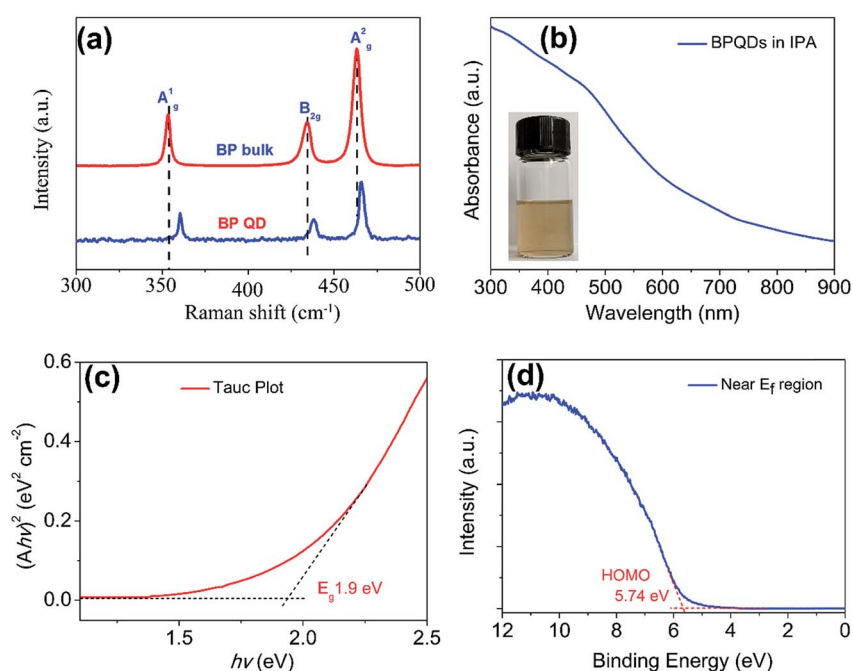
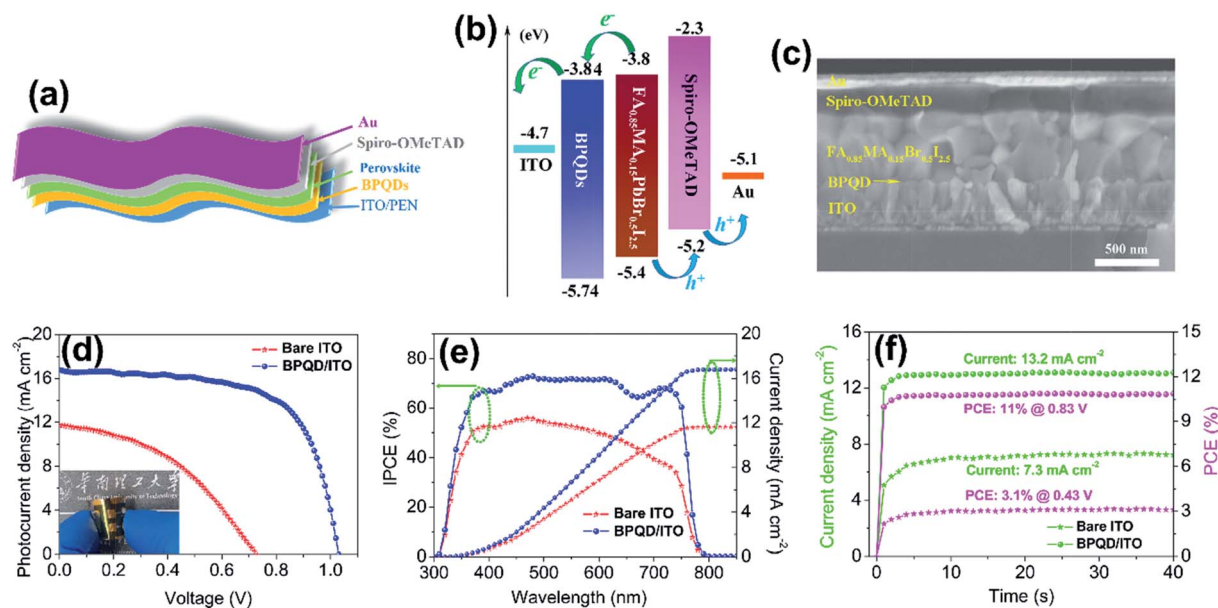


Fig. 2 Optical characterization of black phosphorus quantum dots (BPQDs). (a) Raman spectra of BPQDs and bulk crystalline BP; (b) UV/Vis absorption spectrum of BPQDs in IPA. Inset is the digital photo of the BPQD suspension with high concentration; (c) Tauc plot for the corresponding absorption spectrum presented in (b); (d) UPS spectrum showing the valence band of BPQDs.



**Fig. 3** (a) Schematic illustration of the plastic organic–inorganic perovskite solar cells in this work; (b) energy level diagram of each component of PSCs; (c) cross-sectional SEM image showing the functional layers of the PSCs; (d)  $J$ – $V$  characteristic curves of PSCs built on BPQD electron-selective layer (ESL) and bare ITO substrate, measured under 1 sun illumination ( $100 \text{ mW cm}^{-2}$ ) in a reverse scan (inset, the digital image of the plastic PSC); (e) IPCE spectra and integrated  $J_{\text{sc}}$  curves of PSCs built on BPQD ESL and bare ITO substrate; (f) stabilized power output of the devices constructed on BPQD ESL and bare ITO, measured by keeping the cells at a fixed voltage near the maximum power point on the  $J$ – $V$  curves.

the ESL with five layers of BPQDs exhibits a much higher short-circuit current density ( $J_{\text{sc}}$ ) of  $16.77 \text{ mA cm}^{-2}$ , an open-circuit photovoltage ( $V_{\text{oc}}$ ) of 1.03 V, and a fill factor (FF) of 0.652, achieving a PCE of up to 11.26%, which is more than three times the efficiency of the device without an electron-selective material.

Incident photon-to-electron conversion efficiency (IPCE) measurements were conducted to demonstrate the significant improvement of the device performance. As depicted in Fig. 3e, the device without ESL exhibits a relative low IPCE. In contrast, remarkably higher IPCE values were obtained in the device employing BPQDs (5 layers) as ESL over the entire measurement wavelength range of 300–800 nm. The  $J_{\text{sc}}$  values integrated from the IPCE results are 11.28 and  $16.37 \text{ mA cm}^{-2}$  for the PSCs without and with BPQD ESL, respectively, which are in good agreement with those obtained from the  $J$ – $V$  tests. To assess the reliability of the extracted  $J_{\text{sc}}$  and PCE from the  $J$ – $V$  curves, we examined the stabilized power output (SPO), in terms of photocurrent density as a function of time, by recording the photocurrent over a bias at the fixed maximum power point for

40 s. As illustrated in Fig. 3f, the device constructed on the bare ITO/PEN substrate shows a stabilized photocurrent of around  $7.3 \text{ mA cm}^{-2}$  and a stable PCE of about 3.1%, corresponding to a relatively low SPO-to-PCE ratio (SPO ratio) of 88%. In contrast, the PSC built on the BPQD ESL (5 layers) yields a steady photocurrent of about  $13.2 \text{ mA cm}^{-2}$  and a PCE of around 11%, resulting in a substantially improved SPO ratio of 97.7%. The higher SPO ratio of BPQD-based PSCs might stem from the more efficient extraction and transport of photogenerated electrons from absorber to collective electrode by the BPQD ESL. Additionally, we also study the performance of low-temperature-produced BPQD ESL for rigid PSCs built on FTO/glass substrate. The rigid PSCs with BPQD ESL yields a much higher  $J_{\text{sc}}$  of  $18.49 \text{ mA cm}^{-2}$  and a PCE of 14.6% (Fig. S4 $\dagger$ ), which is not much far behind that of a rigid PSC based on an annealed ( $450 \text{ }^\circ\text{C}$ )  $\text{TiO}_2$  compacted electron transport layer (17.9%, Fig. S5 $\dagger$ ).

In order to improve the PCE of a PSC, a compact ESL is essential to extracting the photogenerated electrons while impeding the hole transfer from the excited perovskite absorber to the collective electrode, thus inhibiting direct carrier recombination (radiative recombination) at the ITO interface. The morphology of ESL films with BPQDs of various thicknesses were observed by SEM and AFM. As revealed by the SEM images (Fig. S6a–c $\dagger$ ), the bare ITO surface with granular grain is covered gradually by BPQDs as the number of coating layers increased. A smooth and dense surface without obvious BPQD aggregation is finally achieved when five layers of BPQDs with a thickness around 30 nm were deposited. However, further increase of the number of layers, e.g. to 7 layers, leads to severe aggregation of the BPQDs (Fig. S6d $\dagger$ ). The 3D AFM images shown in Fig. S7 $\dagger$  reveal that the root-mean-square roughness ( $R_{\text{q}}$ ) of BPQD-

**Table 1** Photovoltaic parameters of the PSCs constructed on the ITO/PEN substrate with BPQD layers of different thicknesses as electron-selective layer

Device	$J_{\text{sc}}$ [ $\text{mA cm}^{-2}$ ]	$V_{\text{oc}}$ [V]	FF	PCE [%]	$R_{\text{s}}$	$R_{\text{sh}}$
Bare ITO	11.71	0.728	0.421	3.58	369	4070
BPQD-1	14.69	0.894	0.483	6.46	214	7737
BPQD-3	15.98	0.945	0.581	8.77	166	18 750
BPQD-5	16.77	1.03	0.652	11.26	58	29 948
BPQD-7	15.76	0.897	0.552	7.81	362	4055

coated electrode decreases from the 4.2 nm of bare ITO to 1.86 nm upon increasing the number of layers from 0 to 5, indicating the formation of smooth BPQD films. In our case, the formation of dense BPQD films (5 layers) on the ITO surface provides an efficient electron transport pathway (low total series resistance,  $R_s$ , Table 1), thus significantly reducing direct charge recombination and leading to the remarkable enhancement in FF and  $V_{oc}$ . The suppressed charge recombination also results in reduced charge loss and boosts the  $J_{sc}$  and PCE.

### 3.3. Morphological and structural quality of the perovskite films

It is reported that the trap-assisted, non-radiative charge recombination plays a dominant role in the efficiency loss in PSCs.<sup>3,48,49</sup> The existence of traps is strongly correlated with the disorder of the grains, which is caused by ionized impurities, lattice vacancies and grain-boundary defects within perovskite films.<sup>49,50</sup> Therefore, control over morphology and crystallinity of perovskite film is of decisive importance in achieving high-performance PSCs.<sup>3,51</sup> Fig. 4 shows the typical SEM images of the perovskite films deposited on the bare ITO surface and BPQD film-coated ITO surface. As depicted in Fig. 4a and b, perovskite film deposited on bare ITO surface shows a random stacking of perovskite nanoplates, surrounded by some phases with indefinite appearance, exhibiting obscure grain boundaries. The X-ray diffraction (XRD) pattern (Fig. 5) of the perovskite film deposited on bare ITO reveals the existence of a large amount of  $PbI_2$ , which may be the phase surrounding the perovskite grains. Herz's work confirmed that the trap-assisted recombination could be greatly accelerated by the presence of composition inhomogeneity in

this disordered region.<sup>49,50</sup> According to the XRD patterns, the perovskite film grown on the BPQD ESL contains around 2 times less  $PbI_2$  compared with that deposited on bare ITO surface. Usually, a moderate residual of  $PbI_2$  can deliver stable and high-efficiency PSCs, while too much  $PbI_2$  in the active film leads to poor transit stability and deteriorates cell performance.<sup>52</sup> Moreover, there are also a number of voids and pinholes in the perovskite film deposited on the bare ITO surface, which will create severe shorting sites for direct charge recombination and lead to a significant efficiency loss as well.<sup>50</sup> For the  $FA_{0.85}MA_{0.15}PbI_{2.5}Br_{0.5}$  film coated on the BPQD ESL, the grains with a size of 100–500 nm were densely packed without observable pinholes and voids (Fig. 4c and d). The low-magnification SEM image shown in Fig. 4c further demonstrates a uniform and regular morphology with well-defined grain boundary. The cross-sectional (Fig. 3c) and top-view SEM (Fig. 4d) also reveals that the grains are packed, with ordered orientation and well-defined grain boundaries, suggesting good crystallinity. A comparison of the SEM images of the perovskite deposited on bare ITO, BPQD-coated ITO (Fig. 4), and low-temperature produced,  $TiO_2$ -coated ITO (Fig. S8†) suggests that the BPQD ESL facilitates the formation of perovskite grains with compact stacking, ordered orientation and less surface roughness. We speculate that the obtained BPQDs with excellent crystallinity (shown in Fig. 1d and e) may act as crystal nuclei for the growth of ultrafine perovskite grains. It is well known that the crystallinity of perovskite active domains greatly affects the charge dissociation, transport, and diffusion length and thus determines the final performance of the solar cells.<sup>53</sup> The XRD patterns shown in Fig. 5 confirm an increased crystallinity of the BPQDs/perovskite, as almost all of the diffraction peaks, especially the (110) and (220), show

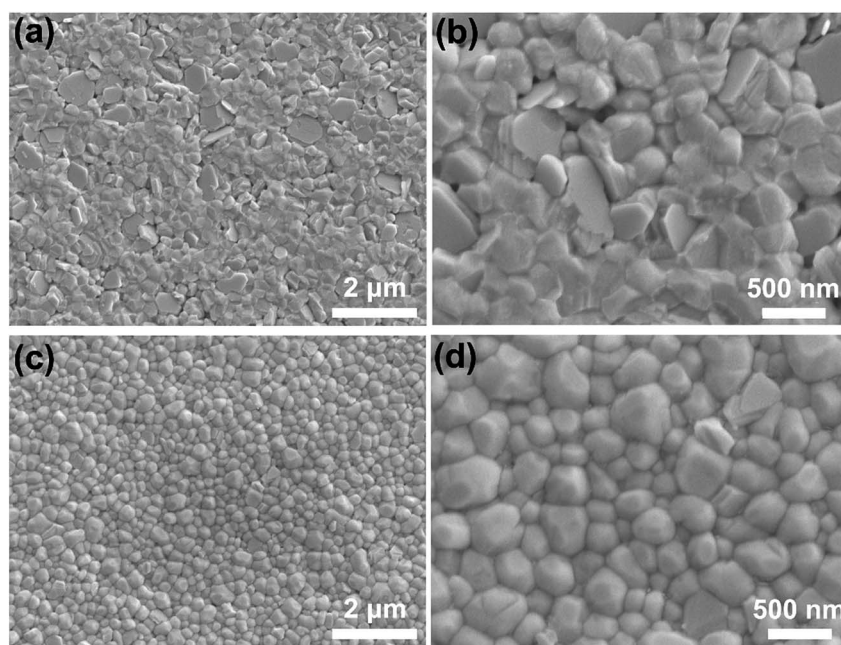


Fig. 4 Perovskite film quality characterization: (a) low-magnification and (b) high-magnification SEM images of perovskite film deposited on bare ITO/PEN substrate; (c) low-magnification and (d) high-magnification SEM images of perovskite film deposited on BPQD-coated ITO/PEN substrate.

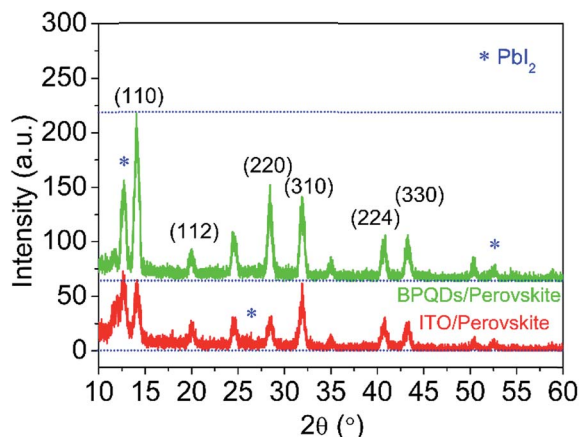


Fig. 5 XRD patterns of  $\text{FA}_{0.85}\text{MA}_{0.15}\text{PbI}_{2.5}\text{Br}_{0.5}$  perovskite deposited on bare ITO/PEN substrate and on BPQD-coated ITO/PEN electrode.

a remarkably increased peak intensity when compared to the bare-ITO/perovskite sample, given that the thickness and the test condition for both films are identical. The strong reflection at  $14.2^\circ$  and  $28.5^\circ$  can be assigned to the (110) and (220) crystal planes of the mixed halide perovskite.<sup>50–53</sup> As compared to other crystal planes, the intensity of (110) and (220) peaks of BPQDs/perovskite is significantly stronger, indicating the texture with the (110) crystal plane is preferentially oriented parallel to the film surface,<sup>53</sup> which is consistent with the observation in SEM measurements. In contrast, no preferential orientation can be observed from both the XRD and SEM tests for the ITO/perovskite film. Therefore, the high-quality perovskite film derived from BPQD film is also responsible for the great improvement in device performance, besides the fast electron extraction mentioned above.

### 3.4 Optoelectronic performance of the perovskite electrodes

To gain further insights into the effects of BPQD ESL on perovskite film quality and charge extraction behavior, the optoelectronic properties of the perovskite film were examined by steady-state photoluminescence (PL) spectrometry and time-resolved PL decay (TRPL). As depicted in Fig. 6, the steady-state PL intensity of perovskite film deposited on BPQD ESL (BPQDs/perovskite) is about four-fold lower than that of perovskite film on bare ITO

substrate, indicating the excellent electron extraction from the absorber by BPQDs. Meanwhile, the steady-state PL peak locates at 762 nm for the BPQDs/perovskite, which shows a smaller Stokes shift compared to that of ITO/perovskite (at 768 nm), demonstrating the milder vibronic relaxation and reduced crystallization defects of the perovskite film on BPQD ESL.<sup>51,54</sup> The charge carrier lifetime was characterized by TRPL to further explore the nature of the significantly improved efficiency of BPQD ESL-based PSCs. The TRPL decay of both BPQDs/perovskite and bare ITO/perovskite exhibit a bi-exponential decay feature containing a fast decay and a slow decay component, as shown in Fig. 6b and Table S2.† It is believed that the fast decay is related to the bimolecular recombination of free charge carriers (electron-hole here) in terms of a direct band-to-band recombination (radiative recombination), while slow decay arises from the monomolecular charge recombination, which predominantly originates from the trapping of charges (non-radiative recombination).<sup>48,49,55</sup> The fast decay is considered to be the result of quenching of the free charges during the charge transport in the perovskite domains and the subsequent transfer into ESL. For the ITO/perovskite film, the fast decay lifetime ( $\tau_1$ ) and slow decay lifetime ( $\tau_2$ ) are 6.8 and 198.2 ns, respectively. The average lifetime ( $\tau_{\text{ave}}$ ) was calculated to be 184.6 ns, according to eqn (1).<sup>56</sup> In contrast, the BPQDs/perovskite film exhibits a significant decrease of  $\tau_1$  and  $\tau_2$  (4.3 ns and 27.6 ns, respectively). Its  $\tau_{\text{ave}}$  (18.3 ns) is one order of magnitude lower than that of the ITO/perovskite sample, indicating the fast transfer of photogenerated electrons from the absorber to the conductive electrode.

$$\tau_{\text{ave}} = \frac{\sum_{i=1}^n A_i \tau_i^2}{\sum_{i=1}^n A_i \tau_i} = \frac{A_1 \tau_1^2 + A_2 \tau_2^2}{A_1 \tau_1 + A_2 \tau_2} \quad (1)$$

$$c_i = \frac{A_i}{\sum_{i=1}^n A_i}, \quad (2)$$

where,  $A_i$ ,  $\tau_i$ , and  $c_i$  are pre-exponential factors, lifetime, and weight concentration for each decay component, respectively.  $\tau_{\text{ave}}$  is the average lifetime of the entire decay process. Here,  $n = 2$  and  $i = 1, 2$ .

The fast electron transfer will result in suppressed radiative recombination, owing to the well-aligned band level and the high charge mobility of dense BPQD film, as well as the obtained high-

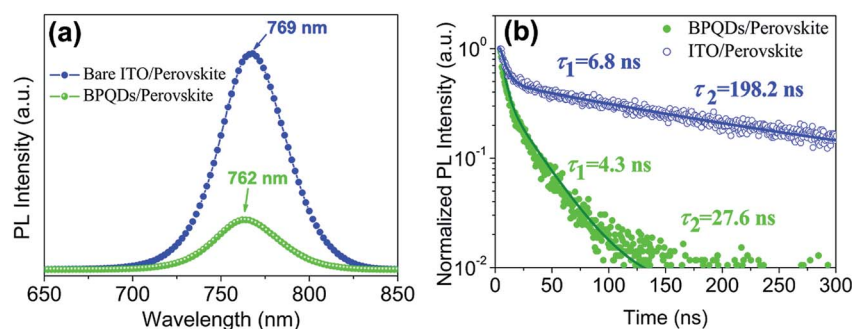


Fig. 6 Perovskite film quality characterization: (a) steady-state photoluminescence (PL) and (b) time-resolved photoluminescence (TRPL) decay trace of the perovskite film deposited on BPQDs/ITO/PNE and bare ITO/PEN substrate.

quality perovskite films.<sup>48,49,53</sup> According to eqn (2),<sup>56</sup> the weight concentration ( $c$ ) for the fast decay component ( $c_1$ ) is 71.1% in the ITO/perovskite sample and 80.3% in the BPQDs/perovskite. The decreased lifetime and increased weight fraction of the fast decay process ( $\tau_1$  and  $c_1$ ) of the BPQDs/perovskite device suggest that most of the photoelectrons generated in the perovskite film are efficiently transferred into the BPQD ESL due to the good electron-extracting capacity of BPQDs and the formation of high-quality perovskite film. The reduction of the trap states and trap-assisted recombination of BPQD ESL-based PSCs can also be confirmed from the photovoltaic characterization. As indicated by the stabilized power output tests (Fig. 3f), the PSCs based on the BPQDs/perovskite takes less than 5 s to generate a stabilized efficiency output, whereas  $\sim 15$  s is required to achieve a stable power output for the device built on bare ITO, indicating the less defects that need to be filled up in the BPQDs/perovskite film. Therefore, we can conclude that the dual-functional BPQDs can act as ESL for fast electron extraction from the perovskite absorber and as an excellent template for the growth of fine perovskite films. The high-quality perovskite film formed on the BPQD ESL suppresses both the radiative and non-radiative recombination, thus reducing charge loss. Consequently, a high efficiency is achieved in the BPQD-based plastic PSCs.

### 3.5 Bending test of the plastic solar cells

Flexibility is a desired feature of plastic solar cells. To assess the flexibility of the BPQD-based plastic device, the obtained device was repeatedly bent with a radius of around 5 mm at a frequency of 1 Hz. The photovoltaic parameter variations as a function of bending cycles are shown in Fig. S9.† It is clear that there are no significant changes in  $J_{sc}$  and  $V_{oc}$  as the bending cycle increased. The SEM images shown in Fig. S10† show no cracks of perovskite films after 200 cycles of bending, indicating that the active layer and even each interface between the functional layers are not damaged by the shape wrench. However, the FF declined remarkably from 0.657 to 0.583, leading to a reduction of PCE from 11.32 to 10.04%, with about 88.7% of the initial PCE being retained. The increased sheet resistance of the ITO/PEN substrate is likely to be the predominant reason for the deterioration of FF and PCE, since the drastic bending can cause cracks to form in the rigid ITO conductive film.<sup>57</sup>

## 4. Conclusions

In summary, we reported the exploitation of solution-processed BPQDs as a novel and dual-functional electron-selective layer for efficient plastic planar heterojunction PSCs. The formation of a well-aligned band cascade between the perovskite absorber and ITO charge collector by the fine BPQDs facilitates the efficient charge extraction and transport. The BPQDs can also facilitate the formation of dense perovskite films with enhanced crystallization. The high-quality perovskite films are pinhole-free and have significantly decreased trap states, which consequently suppresses radiative recombination and trap-assisted, non-radiative recombination in the photovoltaic devices. The low-temperature-produced plastic PSCs employing this newly

developed electron transport material yield a promising power conversion efficiency of up to 11.26%. We believe that further improvement in efficiency can be achieved through chemical modification of BPQDs.

## Conflicts of interest

There are no conflicts to declare.

## Acknowledgements

This work is financially supported by the National Natural Science Foundation of China (Grants No. 61604058) and the Fundamental Research Funds for the Central Universities (2017MS003). This work is also supported by the Science and Technology Research Items of Shenzhen (No. JCYJ20160422102802301 and KQJSCX2016022619562452); the Hong Kong, Macao and Taiwan Science & Technology Cooperation Program of China (No. 2015DFH10200); the project (G1602) of Guangdong Research Center for Interfacial Engineering of Functional Materials, College of Materials Science and Engineering, Shenzhen University; and the Australian Research Council Discovery Project (DP170103514).

## References

- 1 A. Kojima, K. Teshima, Y. Shirai and T. Miyasaka, *J. Am. Chem. Soc.*, 2009, **131**, 6050–6051.
- 2 W. S. Yang, B. W. Park, E. H. Jung, N. J. Jeon, Y. C. Kim, D. U. Lee, S. S. Shin, J. Seo, E. K. Kim, J. H. Noh and S. I. Seok, *Science*, 2017, **356**, 1376–1379.
- 3 M. He, B. Li, X. Cui, B. B. Jiang, Y. J. He, Y. H. Chen, D. O'Neil, P. Szymanski, M. A. El-Sayed, J. S. Huang and Z. Q. Lin, *Nat. Commun.*, 2017, **8**, 16045.
- 4 J. H. Heo, H. J. Han, D. Kim, T. K. Ahn and S. H. Im, *Energy Environ. Sci.*, 2015, **8**, 1602–1608.
- 5 W. Li, W. Zhang, S. V. Reenen, R. J. Sutton, J. Fan, A. A. Haghighirad, M. B. Johnston, L. Wang and H. J. Snaith, *Energy Environ. Sci.*, 2016, **9**, 490–498.
- 6 T. Leijtens, G. E. Eperon, S. Pathak, A. Abate, M. M. Lee and H. J. Snaith, *Nat. Commun.*, 2013, **4**, 2885.
- 7 D. Yang, R. X. Yang, J. Zhang, Z. Yang, S. Z. Liu and C. Li, *Energy Environ. Sci.*, 2015, **8**, 3208–3214.
- 8 N. Q. Fu, Y. Y. Fang, Y. D. Duan, X. W. Zhou, X. R. Xiao and Y. Lin, *ACS Nano*, 2012, **6**, 9596–9605.
- 9 M. Kaltenbrunner, G. Adam, E. D. Glowacki, M. Drack, R. Schwödli, L. Leonat, D. H. Apaydin, H. Groiss, M. C. Scharber, M. S. White, N. S. Sariciftci and S. Bauer, *Nat. Mater.*, 2015, **14**, 1032–1039.
- 10 J. You, Z. Hong, Y. Yang, Q. Chen, M. Cai, T. B. Song, C. C. Chen, S. Lu, Y. Liu, H. Zhou and Y. Yang, *ACS Nano*, 2014, **8**, 1674–1680.
- 11 C. Bi, B. Chen, H. Wei, S. D. Luca and J. Huang, *Adv. Mater.*, 2017, **29**, 1605900.
- 12 Z. Zhu, J. Q. Xu, C. C. Chue, H. Liu, Z. Li, X. Li, H. Chen and A. K.-Y. Jen, *Adv. Mater.*, 2016, **28**, 10786–10793.
- 13 D. Yang, R. Yang, X. Ren, X. Zhu, Z. Yang, C. Li and S. Liu, *Adv. Mater.*, 2016, **28**, 5206–5213.

- 14 J. M. Ball, M. M. Lee, A. Hey and H. J. Snaith, *Energy Environ. Sci.*, 2013, **6**, 1739–1743.
- 15 J. H. Heo, M. H. Lee, H. J. Han, B. R. Patil, J. S. Yub and S. H. Im, *J. Mater. Chem. A*, 2016, **4**, 1572–1578.
- 16 Q. Jiang, L. Zhang, H. Wang, X. Yang, J. Meng, H. Liu, Z. Yin, J. Wu, X. Zhang and J. You, *Nat. Energy*, 2016, **14**, 16177.
- 17 M. Park, J.-Y. Kim, H. J. Son, C.-H. Lee, S. Soon Jang and M. J. Ko, *Nano Energy*, 2016, **26**, 208–215.
- 18 S. S. Shin, W. S. Yang, J. H. Noh, J. H. Suk, N. J. Jeon, J. H. Park, J. S. Kim, W. M. Seong and S. Il Seok, *Nat. Commun.*, 2015, **6**, 7410.
- 19 Y. Hou, C. O. R. Quiroz, S. Scheiner, W. Chen, T. Stubhan, A. Hirsch, M. Halik and C. J. Brabec, *Adv. Energy Mater.*, 2015, **5**, 1501056.
- 20 P. Chen, X. Yin, M. Que, X. Liu and W. Que, *J. Mater. Chem. A*, 2017, **5**, 9641–9648.
- 21 J. Feng, Z. Yanga, D. Yang, X. Ren, X. Zhu, Z. Jin, W. Zi, Q. Wei and S. Liu, *Nano Energy*, 2017, **36**, 1–8.
- 22 V. Nicolosi, M. Chhowalla, M. G. Kanatzidis, M. S. Strano and J. N. Coleman, *Science*, 2013, **340**, 1226419.
- 23 M. Chhowalla, H. S. Shin, G. Eda, L. J. Li, K. P. Loh and H. Zhang, *Nat. Chem.*, 2013, **5**, 263–275.
- 24 H. Liu, Y. C. Du, Y. X. Deng and P. D. Ye, *Chem. Soc. Rev.*, 2015, **44**, 2732–2743.
- 25 X. Zhang, H. M. Xie, Z. D. Liu, C. L. Tan, Z. M. Luo, H. Li, J. D. Lin, L. Sun, W. Chen, Z. C. Xu, L. H. Xie, W. Huang and H. Zhang, *Angew. Chem., Int. Ed.*, 2015, **54**, 3653–3657.
- 26 M. S. Zhu, Y. Osakada, S. Kim, M. Fujitsuka and T. Majima, *Appl. Catal., B*, 2017, **217**, 285–292.
- 27 S. H. Lin, Y. S. Chui, Y. Y. Li and S. P. Lau, *FlatChem*, 2017, **2**, 15–37.
- 28 A. Castellanos-Gomez, *J. Phys. Chem. Lett.*, 2015, **6**, 4280–4291.
- 29 J. P. Lu, J. Yang, A. Carvalho, H. W. Liu, Y. Lu and C. H. Sow, *Acc. Chem. Res.*, 2016, **49**, 1806–1815.
- 30 R. W. Keyes, *Phys. Rev.*, 1953, **92**, 580–584.
- 31 Y. Hou, C. O. R. Quiroz, S. Scheiner, W. Chen, T. Stubhan, A. Hirsch, M. Halik and C. J. Brabec, *Adv. Energy Mater.*, 2015, **5**, 1501056.
- 32 L. Li, Y. Yu, G. J. Ye, Q. Ge, X. Ou, H. Wu, D. Feng, X. H. Chen and Y. Zhang, *Nat. Nanotechnol.*, 2014, **9**, 372–377.
- 33 X. H. Ren, Z. J. Li, Z. Y. Huang, D. Sang, H. Qiao, X. Qi, J. Li, J. X. Zhong and H. Zhang, *Adv. Funct. Mater.*, 2017, **27**, 1606834.
- 34 M. S. Zhu, S. Kim, L. Mao, M. Fujitsuka, J. Y. Zhang, X. C. Wang and T. Majima, *J. Am. Chem. Soc.*, 2017, **139**, 13234–13242.
- 35 M. S. Zhu, X. Y. Cai, M. Fujitsuka, J. Y. Zhang and T. Majima, *Angew. Chem., Int. Ed.*, 2017, **56**, 2064–2068.
- 36 T. Wang, S. Hu, B. Chamlagain, T. Hong, Z. Zhou, S. M. Weiss and Y. Q. Xu, *Adv. Mater.*, 2016, **28**, 7162–7166.
- 37 C. Hao, B. Yang, F. Wen, J. Xiang, L. Li, W. Wang, Z. Zeng, B. Xu, Z. Zhao, Z. Liu and Y. Tian, *Adv. Mater.*, 2016, **28**, 3194–3201.
- 38 J. Sun, H. W. Lee, M. Pasta, H. Yuan, G. Zheng, Y. Sun, Y. Li and Y. Cui, *Nat. Nanotechnol.*, 2015, **10**, 980–985.
- 39 Y. Yang, J. Gao, Z. Zhang, S. Xiao, H. H. Xie, Z. B. Sun, J. H. Wang, C. H. Zhou, Y. W. Wang, X. Y. Guo, P. K. Chu and X. F. Yu, *Adv. Mater.*, 2016, **28**, 8937–8944.
- 40 S. H. Liu, S. H. Lin, P. You, C. Surya, S. P. Lau and F. Yan, *Angew. Chem., Int. Ed.*, 2017, **56**, 13717.
- 41 W. Chen, K. W. Li, Y. Wang, X. Y. Feng, Z. W. Liao, Q. C. Su, X. N. Lin and Z. B. He, *J. Phys. Chem. Lett.*, 2017, **8**, 591–598.
- 42 S. H. Lin, S. H. Liu, Z. B. Yang, Y. Y. Li, T. W. Ng, Z. Q. Xu, Q. L. Bao, J. H. Hao, C. S. Lee, C. Surya, F. Yan and S. P. Lau, *Adv. Funct. Mater.*, 2016, **26**, 864–871.
- 43 T. J. Jacobsson, J. P. Correa-Baena, M. Pazoki, M. Saliba, K. Schenk, M. Grätzel and A. Hagfeldt, *Energy Environ. Sci.*, 2016, **9**, 1706–1724.
- 44 N. Q. Fu, Z. Y. Bao, Y. L. Zhang, G. G. Zhang, S. M. Ke, P. Lin, J. Y. Dai, H. T. Huang and D. Y. Lei, *Nano Energy*, 2017, **41**, 654–664.
- 45 X. Huang, Z. Y. Zeng and H. Zhang, *Chem. Soc. Rev.*, 2013, **42**, 1934–1946.
- 46 Y. Li, Y. Hu, Y. Zhao, G. Shi, L. Deng, Y. Hou and L. Qu, *Adv. Mater.*, 2011, **23**, 776–780.
- 47 S. Das, M. Demarteau and A. Roelofs, *ACS Nano*, 2014, **8**, 11730–11738.
- 48 G. J. A. H. Wetzelaer, M. Scheepers, A. M. Sempere, C. Momblona, J. Ávila and H. J. Bolink, *Adv. Mater.*, 2015, **27**, 1837–1841.
- 49 M. B. Johnston and L. M. Herz, *Acc. Chem. Res.*, 2016, **49**, 146–154.
- 50 W. Rehman, R. L. Milot, G. E. Eperon, C. Wehrenfennig, J. L. Boland, H. J. Snaith, M. B. Johnston and L. M. Herz, *Adv. Mater.*, 2015, **27**, 7938–7944.
- 51 M. Z. Long, T. K. Zhang, W. Y. Xu, X. L. Zeng, F. Y. Xie, Q. Li, Z. Chen, F. Zhou, K. S. Wong, K. Y. Yan and J. B. Xu, *Adv. Energy Mater.*, 2017, **7**, 1601882.
- 52 T. J. Jacobsson, J.-P. Correa-Baena, E. H. Anaraki, B. Philippe, S. D. Stranks, M. E. F. Bouduban, W. Tress, K. Schenk, J. Teuscher, J.-E. Moser, H. Rensmo and A. Hagfeldt, *J. Am. Chem. Soc.*, 2016, **138**, 10331–10343.
- 53 P. W. Liang, C. Y. Liao, C. C. Chueh, F. Zuo, S. T. Williams, X. K. Xin, J. Lin and A. K. Y. Jen, *Adv. Mater.*, 2014, **26**, 3748–3754.
- 54 S. D. Stranks, G. E. Eperon, G. Grancini, C. Menelaou, M. J. Alcocer, T. Leijtens, L. M. Herz, A. Petrozza and H. J. Snaith, *Science*, 2013, **342**, 341–344.
- 55 X. P. Zheng, B. Chen, J. Dai, Y. J. Fang, Y. Bai, Y. Lin, H. Wei, X. C. Zeng and J. S. Huang, *Nat. Energy*, 2017, **2**, 17102.
- 56 B. Valeur, Principles of Steady-State and Time-Resolved Fluorometric Techniques, in *Molecular Fluorescence: Principles and Applications*, Wiley-VCH Verlag GmbH, Weinheim, FRG, 2001, pp. 155–199.
- 57 C. Wang, L. Guan, D. Zhao, Y. Yu, C. R. Grice, Z. Song, R. A. Awni, J. Chen, J. Wang, X. Zhao and Y. Yan, *ACS Energy Lett.*, 2017, **2**, 2118–2124.